

Characterization and Validation of the Heat Storage Variability from TOPEX/POSEIDON at Four Oceanographic Sites

Paulo S. Polito, Olga T. Sato and W. Timothy Liu

Jet Propulsion Laboratory, California Institute of Technology, Pasadena, California

Abstract. Oceanic heat storage and heat storage rate are correlated to the sea surface height anomaly signals from the TOPEX/Poseidon altimeter data from 1992 to 1998. The height anomaly data are decomposed through 2D finite impulse response filtering. The signal components are: the basin-scale non-propagating (seasonal), westward propagating (Rossby waves), eastward propagating (Kelvin waves), meso-scale (eddies), and small-scale (residual). The fractional variance of the components of the altimeter signal establishes a quantitative correspondence between the dynamical processes and the local heat storage variability. Four sites with a nearly continuous time series of temperature profiles of the upper ocean provide data for validation of TOPEX/Poseidon results: TAO, HOT, CalCOFI, and Hydrostation "S". Correlations and rms differences are calculated to compare heat storage estimates based on altimeter and *in situ* data. The heat storage anomaly differences range from 54 to $64 \times 10^7 J m^{-2}$ and the correlations from 67% to 89%. The heat storage rate differences range from 98 to $223 W m^{-2}$ and the correlations from 66% to 73%. The fraction of the variance associated with Rossby waves varies from 13% in the equatorial Pacific to 62% in the tropical North Pacific. Conversely, in the same regions the non-propagating signal goes from 75% to 13%.

1. Introduction

The global energy balance between the atmosphere and the ocean involves dynamic processes that transport heat mostly meridionally and thermodynamic processes responsible for storing and releasing heat as the seasons change. The ocean has a fundamental role in this balance due to its large heat capacity compared to the atmosphere (2.5 m of oceanic water has the same heat capacity per unit area as the entire atmospheric column). The net surface heat flux through the atmosphere-ocean interface results from the balance between the heat locally stored in the ocean, that advected by the oceanic circulation, and that transferred to the atmosphere.

It is important to estimate the oceanic heat storage (HS) to improve our understanding of air-sea interactions and its long-term contribution to climate change. Furthermore, since air-sea heat fluxes estimates are

used to force numerical weather prediction and ocean circulation models there is the necessity of realistic and reliable data.

Estimates of oceanic HS are traditionally based on *in situ* measurements of temperature at specific locations [Yan *et al.*, 1995; Wyrski and Urich, 1982] or on climatological temperature data sets [Hsiung *et al.*, 1989; Moisan and Niiler, 1997]. Most recently, HS has been estimated using altimetry data. White and Tai [1995] derived a linear relationship between the sea level anomaly measured by TOPEX/POSEIDON (T/P hereafter) and the HS estimated from XBT data and found correlations greater than 0.6 over the northern hemisphere. Wang and Koblinsky [1997] assumed simplifications on the buoyancy budget equation of the annual steric height variability to estimate the HS from T/P data and compared it with XBT estimates over the North Atlantic away from the western boundary

and subtropical recirculation regions and found a good agreement.

Chambers *et al.* [1997] estimated the HS anomaly as a linear function of the satellite altimeter measurements of sea level. They showed that the interannual heat storage rate (HSR) estimated from T/P agrees with those from TAO measurements in the tropical Pacific within 5 to 10 W m^{-2} . They also used the average HSR over the basins to infer changes in the mean heat flux between the atmosphere and the ocean. Chambers *et al.* [1998] used the same method to measure HS changes in the equatorial Pacific in comparison with direct measurements from Tropical Ocean-Atmosphere (TAO) buoys. They found good agreement in some cases but not all. Their conclusion was that this resulted from discrepancies between *in situ* and climatological salinities.

One of the problems that one faces when using satellite altimeter data to estimate the HS is that it measures the total sea level anomaly, with contributions from many different phenomena. The objective of this study is to estimate the HS using T/P data, identifying the contributions from the thermal and dynamical processes involved in the HS mechanisms. In addition, the HS and HSR are estimated from *in situ* data and compared to the results based on remotely sensed data.

In the next Section we describe how the HS is estimated from both methods. In Section 3 we present the data, the main points of its processing and address potential problems. Details of the filtering technique applied to the T/P data to decompose it into wave components are presented in Appendix A. In Section 4 we compare the HS and the HSR estimated from the two independent methods. Finally, Section 5 summarizes the main points of this study.

2. Theoretical considerations

2.1. Sea surface height anomaly

Various dynamical and thermodynamical effects contribute to the observed sea surface height anomalies [Gill and Niiler, 1973]. Firstly, tides and the inverse barometer effects which are of little interest to this study. Thus, they are excluded in the early steps of the data processing, as part of the standard T/P corrections. Second, the barotropic response to variable wind forcing, which contributes relatively little to the global sea level variability. Furthermore, this contribution is confined to high latitudes where a time-dependent Sverdrup balance may hold [Fu and Davidson, 1995]. Nevertheless, as the barotropic component is present in the T/P data and absent in the *in situ* data, it is regarded

as a potential source of discrepancies. Third, there are height anomalies due to vertical displacement of the isopycnals. Both salinity and temperature anomalies result in changes in sea level but only the latter reflect a change in the heat storage. Therefore, the salinity effects must be taken into account.

The assumption of conservation of heat for a vertical column of water in a fixed location implies, through Gauss' theorem, that the heat storage rate equals the integrated heat flux through the surfaces. Although very slowly, the bottom surface exchanges heat with the ocean floor. Heat is also advected through the sides of the column by horizontal currents. In addition, the surface exchanges sensible and latent heat with the atmosphere. Regardless of source, if heat enters the water column, it will decrease its density and increase its height, causing a local anomaly. Therefore the sea surface height variations reflect, to a large extent, the amount of heat locally stored in the water column.

2.2. Heat Storage

Heat storage is the energy necessary to raise the temperature from 0 K to the observed temperature at a specific point in the water column:

$$HS = \rho C_p \int_{-h}^0 T(z) dz, \quad (1)$$

where ρ is the density of the seawater, C_p is the specific heat at constant pressure, $T(z)$ is the observed temperature profile, and h is the depth to which the temperature profile is integrated. HS is expressed in units of J m^{-2} .

Ideally, the temperature profiles should be integrated to the ocean bottom to account for the total heat storage in the water column. However, most of the heat related changes observed in the ocean can be correlated to changes in the upper layer. In addition, not many full-depth *in situ* measurements are available. Therefore, the temperature profiles are integrated to a depth below the main thermocline.

To compare with the heat storage anomaly (HS') derived from T/P the *in situ* HS' is obtained from HS minus its local long-term mean. This mean is calculated using the maximum number of integer years available.

The oceanic HSR, expressed in W m^{-2} , can be estimated through:

$$HSR = \frac{\partial HS'}{\partial t}, \quad (2)$$

The T/P sea height anomaly (η_o) can be used to estimate the heat storage anomaly (HS') according to

the linear relation derived by *Chambers et al.* [1997]:

$$HS' = \frac{\rho C_p}{\alpha} (\eta_o + \eta_h). \quad (3)$$

where α is the thermal expansion coefficient. The effects of the haline contraction (η_h) on the sea height anomaly are taken into account. The HSR estimated using the altimeter data is determined by differentiating HS' in time.

Mean values of ρ and C_p , averaged from the surface to a depth h , are calculated from climatological maps of the World Ocean Atlas 1994 (WOA94) [Levitus and Boyer, 1994] for a $1^\circ \times 1^\circ$ grid and then averaged zonally for each oceanic basin. α is considered constant at each grid point and it is estimated by averaging from the surface to a depth h the climatological α profile weighted by the layer thickness and temperature. η_h at each grid point is estimated by vertically integrating from the surface to a depth h the product of the climatological haline contraction coefficient, β , and the salinity anomaly (residual after subtracting the annual mean) profiles. The salinity correction is treated in detail in *Sato et al.* [1999].

2.3. Separating the T/P signal into components

Two features are common to plots of $\eta_o(x, t)$ at most latitudes: the seasonal basin-scale variability and the meso- to large-scale westward propagating signal. These two features portray different physical processes. The basin-scale signal is largely due to a balance between the air-sea surface fluxes, oceanic HS, and the heat advected by ocean currents. The propagating signal varies significantly in spatial scale from the Equator to the poles and its temporal scale is on the order of months to years. Temporal and spatial scales indicate that these anomalies are mostly long first-mode baroclinic Rossby waves [Chelton and Schlax, 1996; Polito and Cornillon, 1997] and arise from a balance between vortex stretching and planetary vorticity. The Rossby waves signal can be detected at the surface because their displacement of the isopycnals changes the vertically averaged density of the water column and therefore causes perturbations in the sea surface height.

Many other dynamical processes contribute to the variability in the sea surface height besides Rossby waves: meso-scale eddies (e.g. rings, lenses), meandering currents, instability waves and Kelvin waves to cite a few. Including all processes the sea surface height anomalies can be described as the following sum:

$$\eta_o = \eta_{t1} + \eta_W + \eta_R, \quad (4)$$

where η_{t1} is the non-propagating basin-scale thermosteric signal, η_W is the westward propagating signal, and η_R is the residual variability which contains a variety of signals, some of which will be of further interest. The westward propagating signal is subdivided into several bands with periods centered at approximately 24, 12, 6, 3, and 1.5 months. Equation 4 becomes, using a suitable notation:

$$\eta_o = \eta_{t1} + \eta_{24} + \eta_{12} + \eta_6 + \eta_3 + \eta_1 + \eta_R. \quad (5)$$

In most latitudes a component of η_R has spatial and temporal scales larger than those of the local Rossby waves. This large-scale signal (η_{t2}) complements the basin-scale signal (η_{t1}). While η_{t1} contains mostly the thermosteric signal due to seasonality, η_{t2} seems to include thermal signals advected by currents and variability due to air-sea heat exchange in scales longer than annual. The total thermal signal is expressed as $\eta_t = \eta_{t1} + \eta_{t2}$.

In the equatorial region η_R shows a fast ($\sim 200 \text{ km day}^{-1}$) eastward propagating component with periods on the order of 1 to 3 months. Albeit not as regular as the Rossby waves, this signal is still relatively easy to identify, particularly in the Pacific basin. This signal (η_K) is identified as equatorial Kelvin waves.

The residual of $\eta_R - \eta_{t2} - \eta_K$ can be broken into meso-scale (η_E) and small scale (η_r) eddy fields. Especially outside the tropical regions the meso-scale eddy signal (η_E) has considerable amplitude with variable temporal and spatial scales. Furthermore, this signal can be influenced by artifacts of the altimeter's sampling strategy. These effects are addressed in Sections 3.3.2 and 3.3.1. η_r is the residual height signal dominated by small scale or high frequency signals and instrument noise. In this context, Equation 5 becomes:

$$\eta_o = \eta_t + \eta_{24} + \eta_{12} + \eta_6 + \eta_3 + \eta_1 + \eta_K + \eta_E + \eta_r. \quad (6)$$

3. Data sources and treatment

3.1. Description of the *in situ* data

Heat storage estimates from *in situ* measurements are compared with estimates using T/P altimetry data at several locations, Figure 1. Fixed stations were preferred because they provide a long time series at point-measurements as opposed to XBT or CTD sections which are not always repeated at the same place or done continuously in time.

The data sources are the buoys from the TAO array in the equatorial Pacific [McPhaden, 1995]; hydrographic sections from the California Cooperative

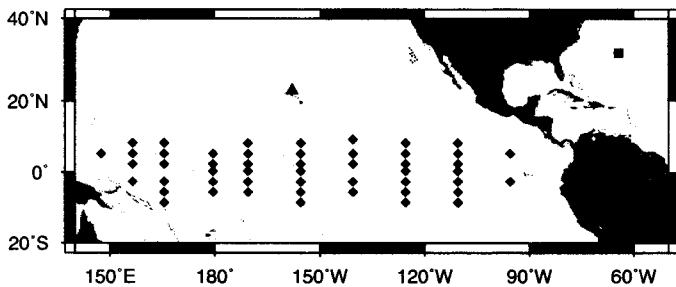


Figure 1. Location of the *in situ* data. Diamonds represent the TAO buoys, triangle the HOT station, square the Hydrostation "S" and dots the CalCOFI cruises.

Table 1. Data source, number of stations used (N), average sampling rate and their location.

Source	N	Rate (days)	Location
TAO	50	1	8°S – 9°N, 140°E – 95°W
CalCOFI	11	90	29.5°S – 35°N, 116°W – 124°W
HOT	1	40	22°N, 158°W
Hydrostation "S"	1	14	32.2°N, 64.5°W

Oceanic Fisheries Investigations (CalCOFI) cruises at the California coast [Lynn and Simpson, 1987]; hydrostation ALOHA from the Hawaii Ocean Time-series Program (HOT) in Hawaii [Karl and Lukas, 1996]; and hydrographic time series near Bermuda sometimes referred to as the Panulirus Station (Hydrostation "S") in the western Atlantic [Schroeder and Stommel, 1969]. The time span, the number of stations, and the sampling rate are different for each source (Table 1). We are interested in a comparison with T/P estimates, therefore only periods common to both sources are considered.

The general procedure consists of linearly interpolating individual temperature profiles in the vertical. Missing surface data (above 25 m) were extrapolated by repeating the first measured value upwards. The underlying assumption is that the missing data were within the mixed layer. Missing data in the deepest

part of the profile (below the main thermocline) were extrapolated using the local mean gradient.

The TAO array provides daily averaged temperature profiles at fixed depths from 75 buoys. Twenty five stations were discarded because of large data gaps. The stations reach 500 m in depth and the HS' was estimated within the upper 300 m. This depth gives the best agreement with the remotely sensed estimates. This implies that the variations observed in the upper layer, above the main thermocline, are mostly responsible for the sea surface variations. For comparison purposes the TAO time series daily samples were averaged for every period of 10 days centered to match the date of the T/P maps.

The CalCOFI data were sampled as deep as 500 m and the HS' was estimated within the top 300 m of the water column. The temporal resolution of the CalCOFI data is the lowest considered for this study (Table 1). Consequently the T/P data was interpolated to match the same dates as the CalCOFI time series.

The HOT program consists of stations located in several sites in Hawaii, however only the station ALOHA was located in an open sea region deep enough (1000 m) for the HS' comparison. HS' was integrated to 500 m. This time series was interpolated to one point per month and compared to a monthly averaged T/P heat storage anomaly.

The Hydrostation "S" near Bermuda has temperature profiles from the surface to 2600 m and the HS' was integrated to 650 m. The time series was interpolated to a resolution of 30 days and compared to monthly averaged T/P estimates.

3.2. Treatment of the altimeter data

3.2.1. Data Description The T/P data used in this study are those distributed by the Jet Propulsion Laboratory Physical Oceanography Distributed Active Archive Center (JPL/PODAAC) published for the World Ocean Circulation Experiment conference (WOCE global data, version 1.1, 1998). The data consist of sea surface height anomalies in relation to a 5-year average (1993-1998) and are presented in bin-averaged grid maps of $0.5^\circ \times 0.5^\circ \times 10$ days. The data cover latitudes between approximately 66° S and 66° N, and from October 1992 to December 1998. All the standard corrections are applied [Benada, 1997]. Details concerning this part of the procedure are found in the documentation distributed with the data.

The sea surface height anomaly is interpolated to a $1^\circ \times 1^\circ$ grid by a bicubic interpolator. Maps of the in-

terpolated sea surface height anomaly, $\eta_o(x, y)$, which are available for every 10 days are converted to Hovmöller diagrams of $\eta_o(x, t)$, one for every degree of latitude (where x and y are the longitude and latitude and t is the time). Data over shallow areas (depth $H \leq -1000\text{m}$), small islands ($x \leq 3^\circ$) and zonally enclosed water bodies are excluded to facilitate filtering. Only continuous open-ocean areas with zonal dimension in excess of 20° , long enough to apply the filter, are used. The basins are separated into Pacific, Atlantic and Indian.

3.3. Potential problems

3.3.1. Tidal Aliasing: temporal undersampling

Tidal aliasing is a potential problem caused by the temporal undersampling of the remainder of the tidal signal left in the T/P record after the model tides are removed. The amplitude of the aliased signal depends on the mismatch between the model and observed tides. Although relatively small in amplitude, this signal may propagate to the East or to the West and therefore be misidentified as a wave if the period and phase speed happen to be similar to the actual waves at a given latitude.

Schlag and Chelton [1994] calculated the aliased periods and wavelengths for the major tidal constituents. Table 2 shows the designation of each tidal constituent, its amplitude relative to M_2 , the period of the aliased signal which can potentially be mistaken as a Rossby (or instability) wave, the wave band, and the latitude where the problem may occur. These latitudes change from basin to basin because the phase speeds of the wave components vary, therefore the table shows the approximate maxima and minima.

The annual and biannual Rossby wave signals cannot be confounded with the aliased tides. The filtering of the westward propagating signals is restricted to the latitudinal bands shown in Table 2. The majority of the aliasing problems affect η_1 . Even within the latitudinal limits it still can be influenced by the M_2 , O_1 and N_2 tides. The latter is of relatively small amplitude and poses a minor problem in the North Equatorial Atlantic. For the Pacific basin the potentially problematic latitudes are near 10° , just outside the TAO region and 20° , near Hawaii.

3.3.2. Rossby Wave Aliasing: spatial undersampling The tidal signal can be aliased because the tidal period is smaller or comparable to twice the temporal sampling rate. Analogously, Rossby waves can be aliased whenever the wavelength is similar or smaller than twice the track separation. While the first effect (tidal alias) is caused by temporal undersampling, the

second (Rossby wave alias) is caused by spatial undersampling.

Wave aliasing depends on the relation between zonal wavelength and zonal track separation. Ascending and descending satellite tracks are combined into single maps such that the average longitudinal distance between samples varies between one and one-half of the track separation. The maximum separation occurs at crossover latitudes. The track separation depends only on latitude whereas the wavelength varies with region, basin, and spectral band. Thus, a wave that is aliased in a given part of the ocean may not be aliased in another location even if the latitude and frequency are the same.

For a fixed Rossby wave frequency the wavelength decreases with latitude faster than the track separation does. Hence, one can expect that aliasing is more likely to occur at high latitudes than near the Equator. However, the period of the Rossby waves reaching a critical latitude also increases with latitude. Consequently, at higher latitudes Rossby waves with lower frequencies are predominant. This effect tends to attenuate the aliasing: as the latitude increases, the waves that would be aliased reach a critical latitude before its wavelength becomes short enough to be effectively aliased.

To avoid this problem the filter for each frequency was limited to a latitudinal band specific to that frequency. The higher the frequency, the lower the threshold latitudes. These latitudes were obtained empirically by allowing the filter to run for all latitudes. Aliasing is indicated by (a) wavelengths that are short compared to the track separation and (b) sudden changes in phase speed. The adopted thresholds are listed in Table 3.

3.3.3. Limitations of the filtering technique

The finite impulse response (FIR) filtering technique has its pitfalls as any alternative option would have. It has less mathematical formalism when compared for example to decomposition in complex empirical orthogonal functions or Fourier analysis. The filters are designed based on *a priori* knowledge about the signal (*i.e.*, its approximate period and phase speed within a factor of two). This information enters the algorithm as a set of parameters that restricts the filter output to particular areas of the frequency-wavenumber spectrum. The signals outside these areas are treated as generic eddy fields (η_E and η_r) whose dynamics are out of the scope of this study.

For locations close to the continental margins the filter operates with less data and is thus less accurate compared to the open ocean. This problem occurs at any place within less than half a wavelength from the

Table 2. Location of potential tidal aliasing problems: tidal constituent, amplitude relative to M_2 , aliased period, wave band that may be influenced and approximate latitude where the westward phase speeds and periods are similar.

Tide	Amplitude (%)	Period (days)	Band	Lat.
M_2	100	62	η_1	18-22°
K_1	58	173	η_6	40-50°
S_2	47	59	η_1	25-30°
O_1	41	46	η_1	15-18°
P_1	19	89	η_3	30-35°
N_2	19	50	η_1	5-10°

Table 3. Location of potential wave aliasing problems: wave band and latitudinal thresholds for each basin.

Band	Indian	Pacific	Atlantic
η_{24}	52.5°S, 17.5°N	52.5°S, 58.5°N	52.5°S, 58.5°N
η_{12}	47.5°S, 17.5°N	47.5°S, 44.5°N	47.5°S, 47.5°N
η_6	39.5°S, 17.5°N	39.5°S, 39.5°N	34.5°S, 37.5°N
η_3	23.5°S, 17.5°N	25.5°S, 28.5°N	28.5°S, 29.5°N
η_1	13.5°S, 17.5°N	22.5°S, 17.5°N	11.5°S, 15.5°N

border (in space or time). At high latitudes ($> 45^\circ$) the phase speeds and wavelengths become very small (a few degrees) even for η_{24} . Consequently, the dimensions of the filters are reduced to a few grid points and their resolving power decreases. In addition, at high latitudes the barotropic response to wind forcing becomes increasingly energetic. Significantly faster than the baroclinic signals, the barotropic signals are aliased due to the temporal resolution of T/P [Thierney *et al.*, 1999; Stammer *et al.*, 1999]. The filtering procedure identifies the aliased barotropic signals as part of the eddy variability.

At low latitudes the gravest modes (η_{12}, η_{24}) often have wavelengths longer than the basin width. At these latitudes the seasonal signal, which in principle has no latitudinal dependence, may not be distinguished from the fast basin-wide Rossby waves. As η_{t1} is the first band to be filtered, it may retain part of the variability which would otherwise be associated with the low frequency Rossby waves. Furthermore, these band-pass filters have a smooth transition between the pass-band and the stop-bands. Since the bands are relatively wide, contamination between adjacent bands is possible. The Rossby wave filters are applied in order of increasing frequency. Thus contamination generally occurs with energy being transferred from a higher frequency band to a lower one. This problem is minimized by removing the correlated part of each component from all the others. Further details about the filtering procedure are in Appendix A.

4. Results

The HS' and HSR are estimated using *in situ* data from four locations: TAO, Hydrostation "S", HOT, and CalCOFI. These are compared to similar estimates based on satellite altimetry (T/P). The residual height components are shown as evidence that (a) the filter does not significantly change the original data and (b) the filtered components can be identified as waves whose characteristics and dynamics are known to a large extent.

4.1. Equatorial Pacific (TAO)

4.1.1. Composition of the Altimeter Signal

An example of the composition of the T/P altimeter signal for the TAO region is shown in Figure 2 for 4.5°N . Slanted patterns indicate propagation: the same phase can be traced as it progresses in space and time. Two additional fields are shown: the sum of the filtered signals, η_s and the residual $\eta_r = \eta_o - \eta_s$ (Equation 6).

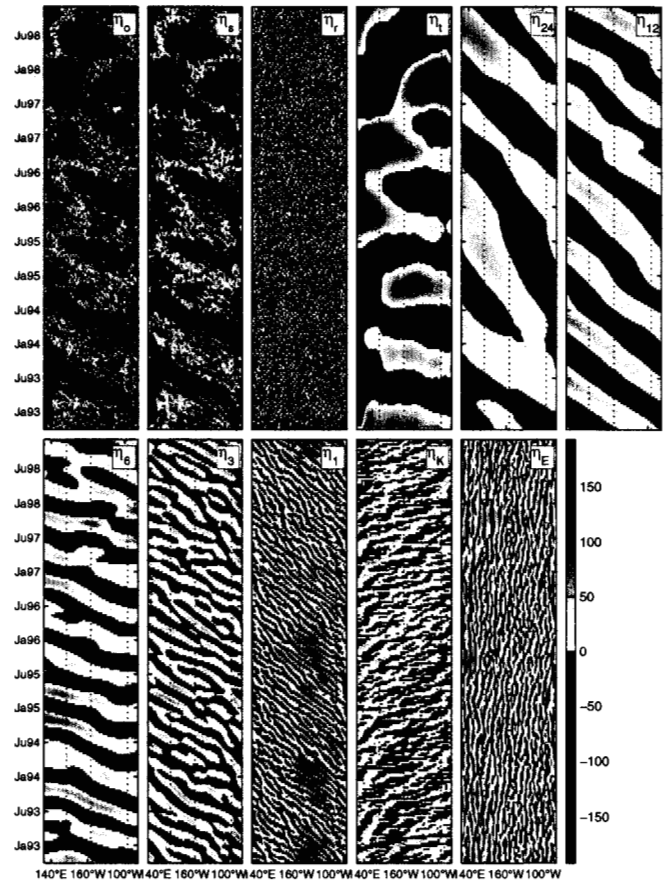


Figure 2. Sea surface height anomalies components (in mm) from T/P as a function of longitude and time at 4.5°N in the Pacific (TAO). The color scale is the same for all plates.

The original data (η_o , top left plate) reveals the presence of several components of the residual height signal. A low-frequency, basin wide signal associated with the El Niño is particularly strong in 1997. The seasonal cycle superimposed on westward propagating waves with nearly annual frequency is ubiquitous. On a temporal scale of approximately two months, westward propagating signals are noticeable in the central-eastern Pacific, stronger between July and January of the years without an El Niño. Filtering allowed a more objective look into the components of the residual height signal. The most important point brought by Figure 2 is that the sum of the filtered fields η_s is a good approximation of the original field η_o , accounting for over 90% of the total variance. This validates the filtering technique as a tool to separate the signal into additive components.

The wave components are characterized by their period T and wavelength L as described in Appendix A. The component maps are divided into as many L by T areas as possible. For each area c_p , T , and A are estimated, the ensemble mean and standard deviation are calculated (Table 4) and estimates outside the 95% confidence level eliminated. A single estimate of the fractional variance (σ) of each component is obtained for the whole basin width and period. The relative importance of each component is illustrated by the two rightmost columns in Table 4: the mean amplitude A and the fractional variance σ . The amount of variance σ explained by η_i is larger than the sum of the wave signals and it grows towards the Equator.

Most westward propagating signals ($\eta_{24,12,6,3}$) can, in principle, be identified as long equatorial Rossby waves [Boulanger and Menkes, 1995]. η_{24} reaches a local maximum in amplitude near 6.5°N . η_{12} has its largest amplitudes away from the Equator, reaching 40 mm at 8.5°N . Within a degree of the Equator the annual signal becomes very weak, explaining only 1% of the total variance. Within 4.5° of the Equator η_6 is generally the strongest signal propagating to the west. Its period however is significantly below 180 days. As a result the amplitude of η_3 is probably underestimated for latitudes below 4.5° . One can speculate that this is the westward propagating response to the arrival of the Kelvin wave signals at the eastern border [Boulanger and Menkes, 1995]. Instability waves reported in the literature [Quiao and Weisberg, 1995] have periods, wavelengths and phase speeds similar to those of η_1 . Figure 2 shows an η_1 whose amplitude is modulated by the seasonal cycle, with a maximum near 6.5°N , 130.5°W . The eastward propagating signal (η_K) has both phase speed and period that match those of equatorial Kelvin waves

and is therefore identified as such.

4.1.2. Comparison of Heat Storage Estimates

Despite the multi-faceted dynamics of the equatorial Pacific, results for this area are encouraging in terms of matching estimates based on remotely sensed measurements to those derived from *in situ* data. One of the reasons for this relative success is that the temporal resolution of the *in situ* data is even higher than that of the altimeter, allowing for averaging that in turn reduces the noise level. In addition, wavelengths are much longer than the distance between T/P samples, reducing the possibility of aliasing.

For the TAO array data, the HS' and HSR are estimated based on equations 1 and 2 respectively. HS' for the T/P data is based on equation 3 including all elements of equation 6 but the small-scale high-frequency dominated residual (η_r). Estimates at four selected buoys are compared to the T/P estimates, Figure 3.

The HS' error based on the error of the temperature measurements in the TAO data alone is $50 \times 10^7\text{ J m}^{-2}$ [Chambers et al., 1997]. In this study, the HS' is estimated with a temporal resolution of 10 days. Nevertheless, the mean rms difference between the T/P and TAO estimates is $54 \times 10^7\text{ J m}^{-2}$. The relatively high

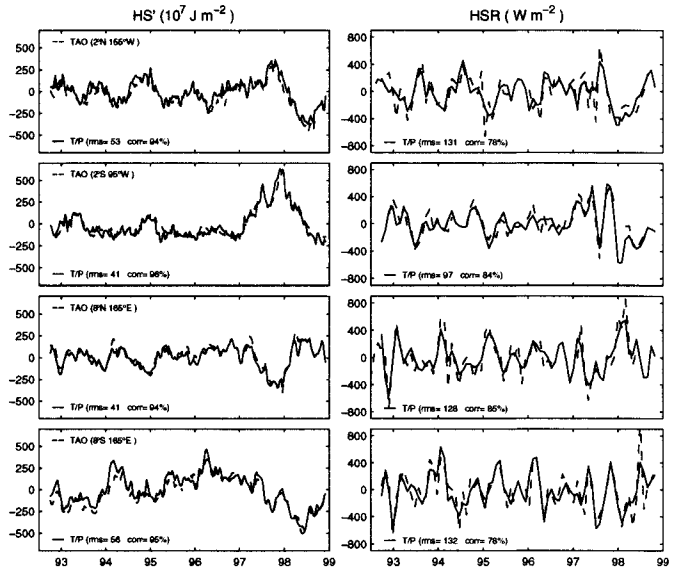


Figure 3. Comparison of the heat storage anomaly (left) and heat storage rate (right) between TAO (dashed) and T/P (solid) at selected buoys. The rms difference and correlation coefficients are shown in the lower left.

Table 4. Wave parameters from T/P in the TAO region in the equatorial Pacific. c_p is the zonal phase speed, T is the period and A is the amplitude. All values are averages in time and zonal dimension followed by the respective standard deviations (zeros indicate insufficient data). σ is the fractional variance.

Lat.	Band	c_p (km day ⁻¹)	T (days)	A (mm)	σ (%)
8.5°S	η_t	64
	η_{24}	-40 ± 5	552 ± 30	17 ± 0	4
	η_{12}	-35 ± 3	375 ± 21	27 ± 3	5
	η_6	-44 ± 11	168 ± 34	24 ± 10	6
	η_3	-38 ± 10	89 ± 18	16 ± 5	3
	η_1	-25 ± 5	53 ± 11	23 ± 7	6
6.5°S	η_t	64
	η_{24}	-37 ± 5	612 ± 22	25 ± 1	5
	η_{12}	-38 ± 4	341 ± 43	25 ± 1	4
	η_6	-51 ± 15	159 ± 25	20 ± 8	6
	η_3	-44 ± 12	81 ± 18	16 ± 5	3
	η_1	-34 ± 8	46 ± 8	23 ± 6	5
4.5°S	η_t	67
	η_{24}	-33 ± 8	642 ± 105	29 ± 10	7
	η_{12}	-45 ± 6	335 ± 31	15 ± 1	2
	η_6	-130 ± 35	102 ± 12	22 ± 12	6
	η_3	-68 ± 22	85 ± 15	17 ± 5	2
	η_1	-39 ± 19	46 ± 9	23 ± 6	4
2.5°S	η_K	202 ± 76	60 ± 10	16 ± 3	2
	η_t	75
	η_{24}	-28 ± 7	729 ± 156	31 ± 13	6
	η_{12}	-46 ± 5	344 ± 25	14 ± 1	1
	η_6	-108 ± 12	101 ± 8	21 ± 9	4
	η_3	-64 ± 19	89 ± 17	15 ± 4	1
0.5°S	η_1	-38 ± 11	44 ± 9	20 ± 4	3
	η_K	179 ± 28	61 ± 10	22 ± 6	3
	η_t	76
	η_{24}	-30 ± 11	756 ± 216	20 ± 3	4
	η_{12}	-49 ± 6	362 ± 44	10 ± 1	0
	η_6	-113 ± 0	95 ± 3	28 ± 12	6
0.5°N	η_3	-110 ± 36	78 ± 10	17 ± 4	2
	η_1	-41 ± 12	44 ± 9	19 ± 4	2
	η_K	182 ± 37	61 ± 11	25 ± 7	4
	η_t	75
	η_{24}	-34 ± 10	714 ± 153	26 ± 10	4
	η_{12}	-43 ± 6	366 ± 45	10 ± 1	1
2.5°N	η_6	-113 ± 0	96 ± 4	27 ± 12	6
	η_3	-101 ± 35	79 ± 10	16 ± 5	2
	η_1	-40 ± 11	45 ± 10	20 ± 4	2
	η_K	194 ± 48	59 ± 11	25 ± 8	4
	η_t	69
	η_{24}	-38 ± 14	669 ± 113	29 ± 2	6
	η_{12}	-47 ± 5	347 ± 22	20 ± 3	2
	η_6	-112 ± 3	101 ± 6	25 ± 9	5
	η_3	-70 ± 23	86 ± 17	15 ± 4	2
	η_1	-38 ± 11	44 ± 10	22 ± 6	4

Table 4. (continued)

Lat.	Band	c_p ($km\ day^{-1}$)	T (days)	A (mm)	σ (%)
4.5°N	η_K	212 ± 70	56 ± 10	22 ± 6	3
	η_t	55
	η_{24}	-30 ± 11	672 ± 222	36 ± 0	6
	η_{12}	-45 ± 4	345 ± 23	35 ± 5	7
	η_6	-146 ± 51	95 ± 15	30 ± 11	7
	η_3	-69 ± 20	87 ± 15	23 ± 6	4
	η_1	-38 ± 9	45 ± 9	30 ± 11	8
6.5°N	η_K	139 ± 20	65 ± 10	22 ± 5	3
	η_t	52
	η_{24}	-37 ± 14	559 ± 190	35 ± 15	8
	η_{12}	-39 ± 2	373 ± 43	42 ± 6	8
	η_6	-55 ± 18	172 ± 31	29 ± 7	6
	η_3	-42 ± 11	80 ± 12	24 ± 7	4
	η_1	-35 ± 8	45 ± 9	33 ± 12	8
8.5°N	η_t	54
	η_{24}	-22 ± 4	682 ± 153	27 ± 6	6
	η_{12}	-34 ± 6	338 ± 58	39 ± 5	9
	η_6	-33 ± 8	208 ± 32	29 ± 3	6
	η_3	-31 ± 8	91 ± 20	24 ± 7	4
	η_1	-25 ± 9	53 ± 12	31 ± 10	7

correlation (89%) shows that even including high frequencies the altimeter and the *in situ* results are very similar.

The HSR (right panel on Figure 3) is calculated with a time differential of 30 days. This time interval helps to counteract the deterioration of the signal to noise ratio due to differentiation. Filtering marginally improved the results ($\sim 1\%$ in correlation and $\sim 10\ W\ m^{-2}$ in rms). The HSR rms difference between both estimates is $149\ W\ m^{-2}$ and the correlation is 70%.

A region of higher values in the rms differences is found in the central Pacific from $140^\circ W$ to $120^\circ W$ north of $5^\circ N$ similar to what *Chambers et al.* [1997] have found (Figure 4). However, the higher values in the warm pool southwest of the equator found in their study is not reproduced in our results. This indicates that the filtering method is able to correlate better the sea level change with the HS' in the upper layer.

The inclusion of a climatological salinity effect did not change the results significantly. The HS' mean rms difference accounting for the salinity effects is $55 \times 10^7\ J\ m^{-2}$ and the correlation is 88%. This suggests that for the TAO region the seasonal fluctuations in the climatological salinity are not the dominant salin-

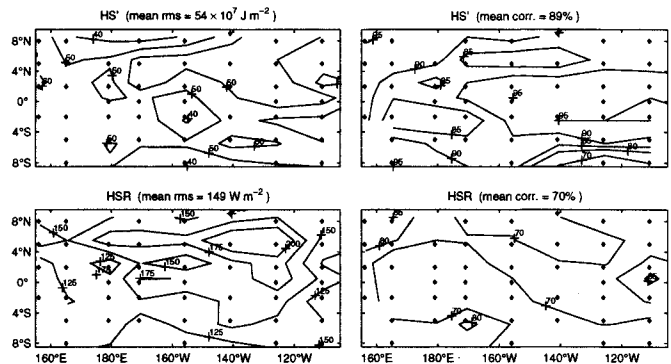


Figure 4. Rms difference (left) and correlation coefficients (right) between TAO and T/P estimates of the heat storage anomaly (top) in $10^7\ J\ m^{-2}$ and heat storage rate (bottom) in $W\ m^{-2}$. Diamonds represent the location of the buoys.

ity signal. This should not come as a surprise given the effects of the El Niño in this region.

4.2. Mid Latitudes Northwestern Atlantic (Hydrostation “S”)

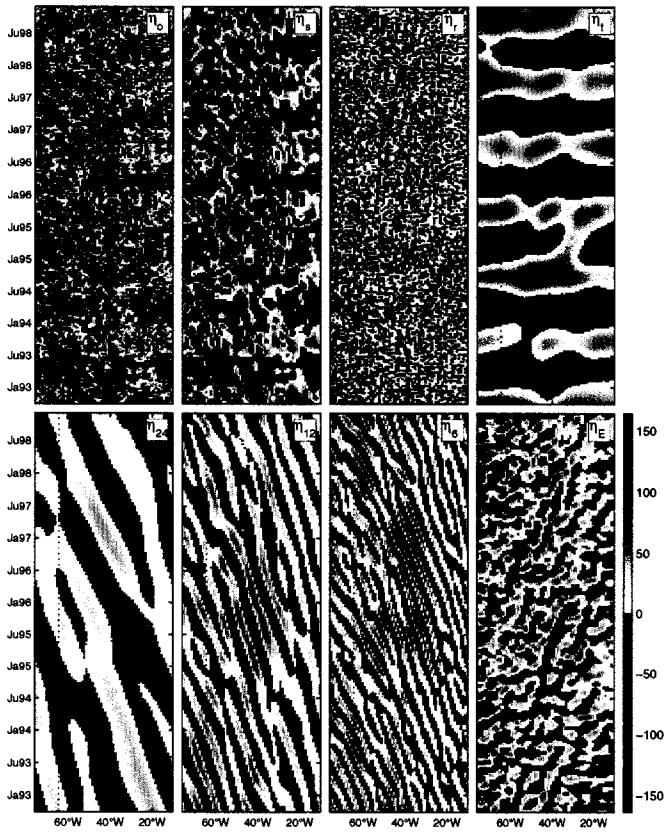


Figure 5. Sea surface height anomalies at 32.5°N (Hydrostation “S”) in the Atlantic, similar to Figure 2.

4.2.1. Composition of the Altimeter Signal

The original and the filtered signals in the sea surface height anomalies along the latitude of 32.5°N are shown as a function of longitude and time in Figure 5. The zonal and temporal variability of the amplitude of the wave fields is evident: both η_{12} and η_6 increase in amplitude west of $\sim 30^\circ\text{W}$ particularly during 1995 and 1996. Propagation is indicated by the slope of the wave field patterns and shows semiannual and annual waves crossing the whole basin at a slightly higher phase speed on the western half of the basin.

The thermal signal and the sum of the propagating signals explain approximately the same amount of variance (Table 5). This is an important result which underlines the importance of Rossby waves for local estimates of the heat budget. The Rossby wave components have average phase speeds similar to previous results [Halliwell and Cornillon, 1989; Schlax and Chelton, 1994; Wang and Koblinsky, 1995; Polito and Cornillon, 1997].

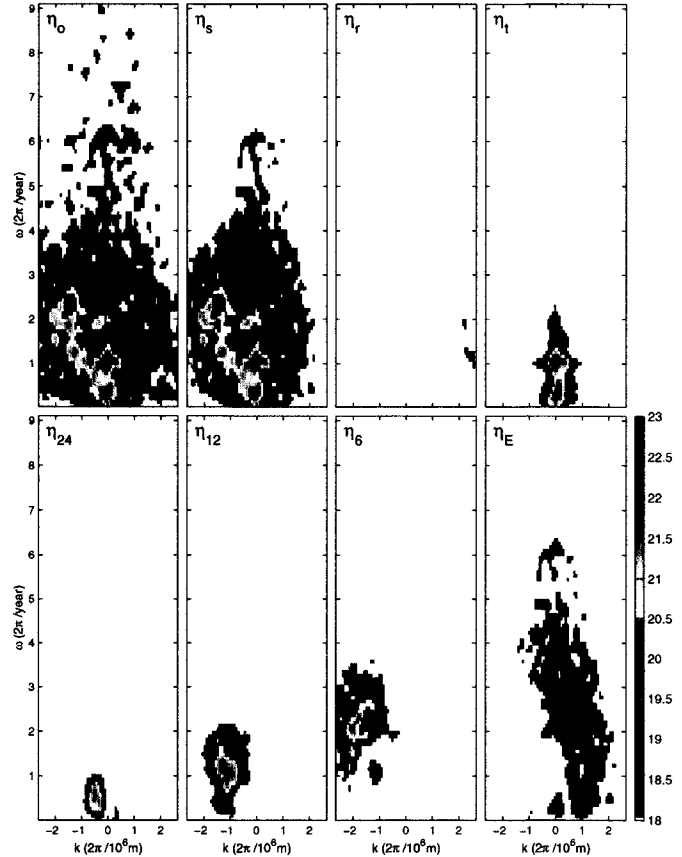


Figure 6. Power spectrum distribution (in db) as a function of zonal wavenumber, k , and frequency, ω , at 32.5°N in the Atlantic (Hydrostation “S”) estimated from T/P sea surface height anomalies. Plate disposition is similar to Figure 5.

Figure 6 shows the zonal-temporal power spectrum density P for the filtered wave components. This is an alternative way to check if the filtering process significantly alters the original signal. The spectrum of the thermal signal, $P(\eta_t)$, shows little indication of propagation ($k = 0$) with just one peak near the annual frequency that extends down to lower frequencies. Westward propagation is indicated by peaks in the left half ($k < 0$) of the plot. The semiannual signal, $P(\eta_6)$, shows a high-energy region from about 1.5 to 2.8 cycles per year while the annual, $P(\eta_{12})$, spectrum spreads near 0.5 and 1.5 cycles per year. $P(\eta_{24})$ is relatively weak and centered at 0.5 cycles per year. The spectrum of the meso-scale eddy signals $P(\eta_E)$ is broader and more diffuse than the Rossby wave spectra. $P(\eta_r)$ has very little energy in the range shown; most of it is in the small-scale, high-frequency range.

Table 5. Wave parameters from T/P for 32.5°N (Hydrostation “S”) in the Atlantic, similar to Table 4.

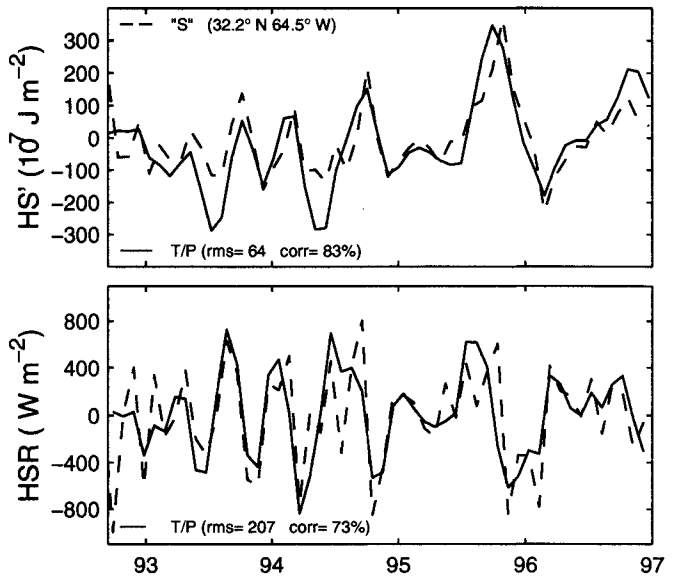
Band	c_p ($km\ day^{-1}$)	T (days)	A (mm)	σ (%)
η_t	35
η_{24}	-3.1 ± 0.5	910 ± 94	28 ± 2	5
η_{12}	-2.5 ± 0.4	349 ± 97	41 ± 16	12
η_6	-3.3 ± 0.9	182 ± 38	39 ± 16	12

Although noisier than the wave spectra, η_E displays noticeable eastward propagation. This effect is due in part to the spatial aliasing (see Section 3.3.2) of η_6 , perceived as a modulation in its amplitude. In Figure 5 the η_o plot shows a modulated crest that starts near 25°W on January of 1995 that can be followed to the west as time progresses. The aliasing of the waves (η_6 in this example) occurs because their wavelength (600 km) is comparable to twice the local track separation (266 km) and 32.5°N is very close to a crossover latitude, 32.37° [Schrama and Ray, 1994]. Therefore, the aliasing should be more pronounced at this latitude compared to the adjacent latitudes. It is indeed the case: both the average amplitude and fractional variance of η_6 at 32.5°N (Table 5) are smaller than their counterparts at 31.5°N (41 mm and 18%) and 33.5°N (72 mm and 23%). The pattern displayed by η_E can be traced back to η_o both in Figure 5 and in Figure 6. This indicates that the eastward propagating signal (wave alias) is part of the original T/P data and not an artifact of the filtering.

4.2.2. Comparison of Heat Storage Estimates

The altimeter-derived HS' includes all elements of equation 6 except the meso-scale eddy signal (η_E) and small-scale residual (η_r). η_E is excluded because it is contaminated by the Rossby waves aliased signal (Sections 4.2.1 and 3.3.2). Figure 7 shows HS' discrepancies relatively larger in the first two years compared to the rest of the series. This is due to semi-annual Rossby waves which dominate the spectrum until late 1994. These waves have a shorter wavelength and are therefore more affected by aliasing than the annual waves which dominate later on.

For Hydrostation “S” *in situ* salinities were used [Sato *et al.*, 1999]. The rms difference between the two HS' estimates is $64 \times 10^7 J m^{-2}$ and the correlation is 83%. A comparison of the two HSRs shows a rms difference of $207 W m^{-2}$ and a correlation coefficient of 73%.

**Figure 7.** Comparison of the heat storage anomaly (top) and heat storage rate (bottom) between Hydrostation “S” (dashed) and T/P (solid).

4.3. Tropical North Pacific (HOT)

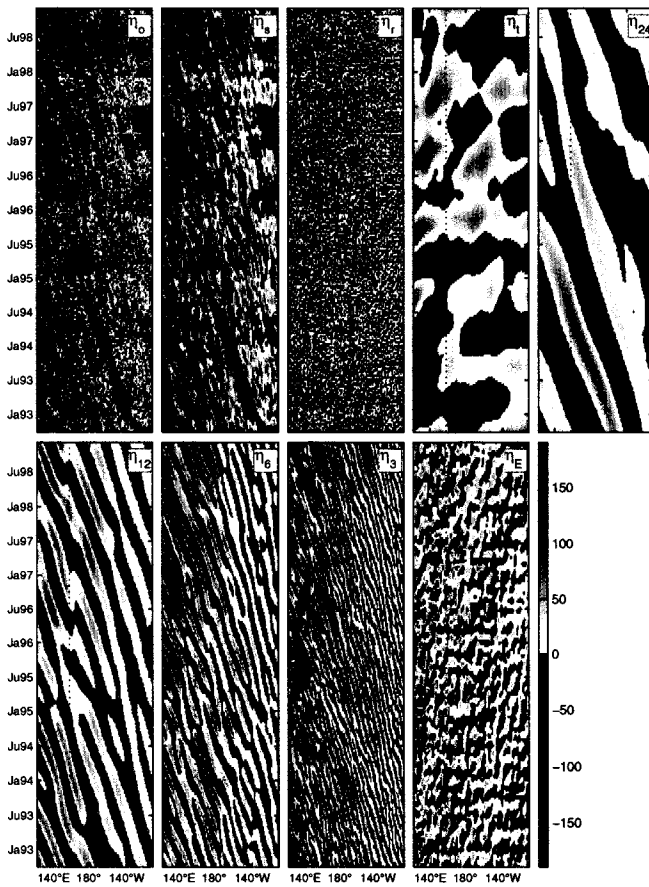
4.3.1. Composition of the Altimeter Signal

Table 6 shows the average parameters for the filtered T/P signal for the HOT location near Hawaii. Further details can be seen in the zonal-temporal diagrams of Figure 8 for 22.5°N, the approximate latitude of the station.

The fractional variance of η_t (Table 6) is a factor of 2 smaller than that of Hydrostation “S” (Table 5), and a factor of 5 smaller than that of TAO (Table 4). The total Rossby wave signal explains over 4 times more variance than η_t . η_6 is the strongest among the westward propagating signals, with an average amplitude of 48 mm and accounting for 23% of the variance. The

Table 6. Wave parameters from T/P for 22.5°N (HOT) in the Pacific, similar to Table 4.

Band	c_p ($km\ day^{-1}$)	T (days)	A (mm)	σ (%)
η_t	13
η_{24}	-6.5 ± 0.7	916 ± 184	45 ± 11	8
η_{12}	-6.8 ± 1.0	372 ± 32	44 ± 21	12
η_6	-6.3 ± 1.3	196 ± 38	49 ± 30	23
η_3	-5.9 ± 1.0	96 ± 14	48 ± 25	19

**Figure 8.** Sea surface height anomalies at 22.5°N (HOT) in the Pacific, similar to Figure 2.

values of c_p in Table 6 are smaller than those reported by Kessler [1989] ($-9.5\ km\ day^{-1}$ for the annual band and $-15.5\ km\ day^{-1}$ for the inter-annual band at 22°N) based on *in-situ* data. Estimates of c_p based on the same instrument [Chelton and Schlax, 1996] yield results statistically identical to the ones in Table 6.

Westward propagating signals are stronger in the Western Pacific than in the Eastern basin (Figure 8). η_E does not show any clear evidence of propagation, suggesting that aliasing should not be a problem at this location. It is interesting to notice that while η_{24} has a larger amplitude before July of 1995, both η_{12} and η_6 show a small yet consistent increase in amplitude after this date. This is an indication that the spectral power distribution at this latitude has changed in time.

4.3.2. Comparison of Heat Storage Estimates

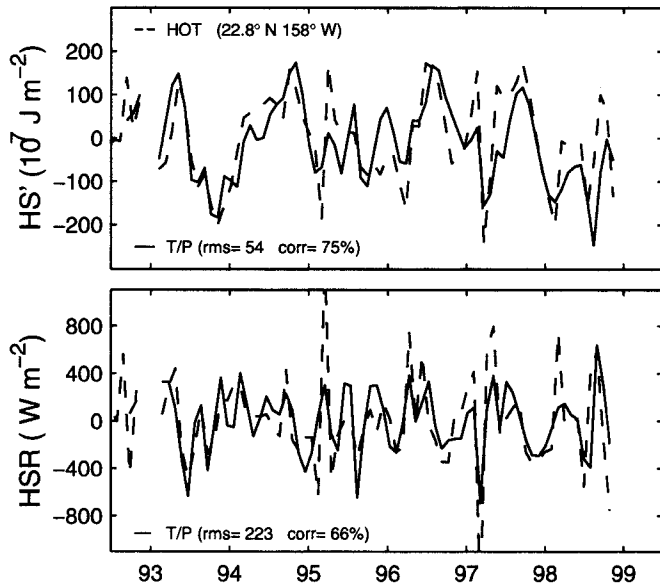
The HS' and HSR from HOT and T/P show reasonable correlations and rms differences, although the results are weaker than those obtained for the TAO estimates. The major source of uncertainty of the HS' estimates derives from the sampling rate of the *in situ* data. The average rate of one sample every 40 days is marginally able to sample η_3 , responsible for 19%. The HSR is a derivative quantity and therefore it is more sensitive to problems related to undersampling.

Figure 9 corroborates this idea: as the high frequencies get relatively stronger after July of 1995, the mismatch between the HS rates get larger. The proximity to the Hawaiian archipelago adds two other factors to be considered in the analysis of these results. One is the possible presence of topographic eddies which none of the instruments can properly resolve. The other is that a gap in the data (land) reduces the number of available points for interpolation and filtering of the T/P data, inducing a local maxima in the statistical errors around the Islands.

The height anomaly due to salinity effects is estimated from *in situ* measurements [Sato *et al.*, 1999]. The rms difference between the hydrographic and altimetric estimates of HS' is $54 \times 10^7\ J\ m^{-2}$ and the correlation coefficient is 75%. Similarly for the HSR the rms difference is $223\ W\ m^{-2}$ and the correlation is 66%.

Table 7. Wave parameters from T/P for the CalCOFI region in the eastern Pacific, similar to Table 4

Lat.	Band	c_p ($km\ day^{-1}$)	T (days)	A (mm)	σ (%)
31.5°N	η_t	31
	η_{24}	-2.8 ± 0.7	1106 ± 264	41 ± 15	7
	η_{12}	-2.8 ± 0.6	415 ± 82	40 ± 26	12
	η_6	-3.3 ± 0.8	181 ± 35	52 ± 39	16
32.5°N	η_t	32
	η_{24}	-2.2 ± 0.6	976 ± 341	46 ± 31	9
	η_{12}	-3.8 ± 0.8	333 ± 80	36 ± 27	7
	η_6	-2.8 ± 0.5	209 ± 45	50 ± 42	17
33.5°N	η_t	27
	η_{24}	-1.9 ± 0.5	768 ± 149	51 ± 34	10
	η_{12}	-3.2 ± 0.7	326 ± 74	44 ± 35	10
	η_6	-2.4 ± 0.5	208 ± 36	57 ± 50	18

**Figure 9.** Comparison of the heat storage anomaly (top) and heat storage rate (bottom) between HOT and T/P, similar to Figure 7.

4.4. Mid Latitudes Northeastern Pacific (CalCOFI)

4.4.1. Composition of the Altimeter Signal

Results of filtering the T/P signal for the CalCOFI location are synthesized in Table 7 and illustrated in Figure 10 for 32.5°N, a latitude within the sampled re-

gion.

The non-propagating signal (η_t) at CalCOFI has a fractional variance similar to that estimated for the Hydrostation “S” (32.5°N in the North Atlantic). The total westward propagating signal explains approximately as much of the variance as the non-propagating. η_6 is the strongest among the westward propagating signals, with an average amplitude above 50 mm and accounting for 17% of the variance. The values of c_p in Table 7 are smaller than those reported by *Chelton and Schlax* [1996] ($\sim 4\ km\ day^{-1}$).

The η_E plate in Figure 10 shows evidence of eastward propagation, illustrating the Rossby wave aliasing problem. This is similar to what was observed for the Hydrostation “S”, discussed in Section 4.2.2.

4.4.2. Comparison of Heat Storage Estimates
CalCOFI is the location with, on average, the smallest correlations and largest rms differences of all *in situ* data sources used in this study. Several factors contribute to the discrepancies. The temporal resolution of one sample every 90 days can barely resolve η_6 . The sampled region extends roughly from 30°N to 34°N and contains a T/P crossover latitude (32.37°N). Therefore η_6 is also marginally resolved at 32.5°N by T/P, with approximately 2.3 samples per wavelength. Because of the Rossby wave aliasing due to the proximity to a crossover point, the wave component η_E is not included in the HS' estimation. However, the most important problem is the degradation of the T/P signal resulting from tide removal, interpolation, and filtering near the continental margin. The correlations consistently decay

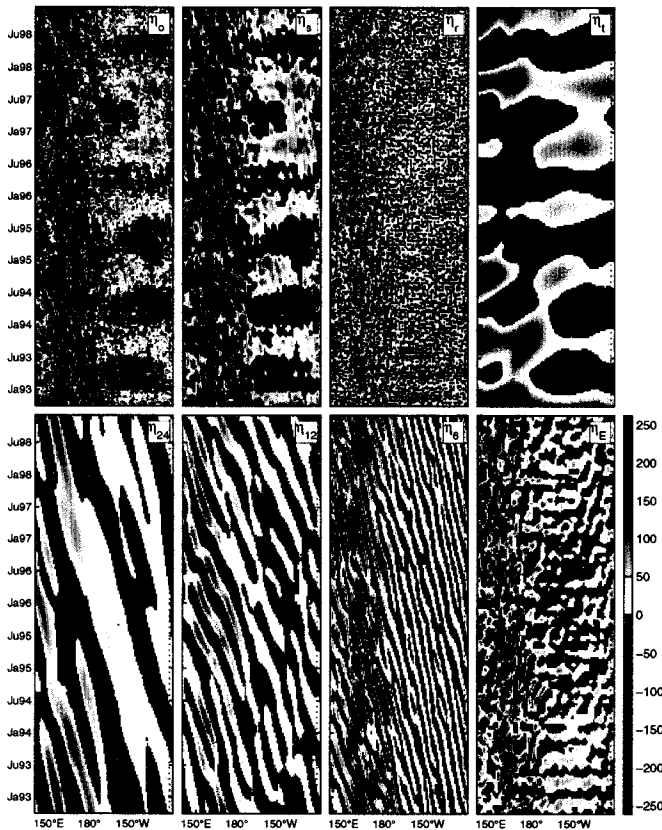


Figure 10. Sea surface height anomalies at 32.5°N (CalCOFI) in the Pacific, similar to Figure 2.

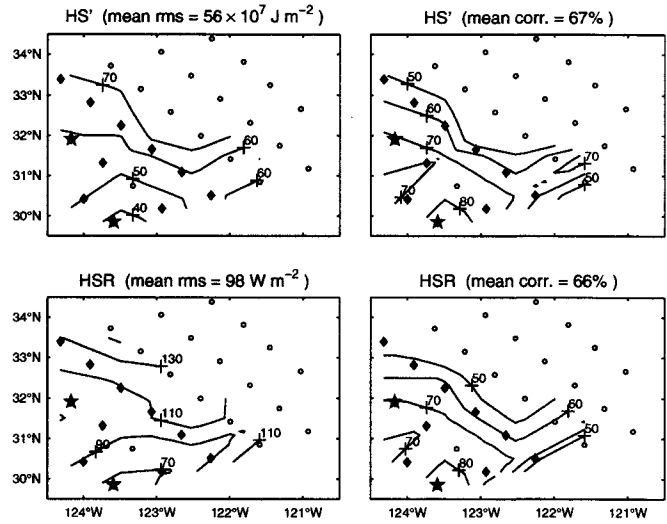


Figure 11. Rms differences (left) and correlation coefficients (right) between CalCOFI and T/P estimates of heat storage anomaly (top) in $10^7 J m^{-2}$ and heat storage rate (bottom) in $W m^{-2}$. Diamonds (circles) mark the location of the used (discarded) stations. Stars correspond to stations in Figure 12.

with the proximity to the coast (Figure 11). Thus all stations close to the continent were excluded. In addition, station 90/110 located at 30.75°N, 123.33°W gave results which were de-correlated with all stations in its vicinity and was also excluded from the analysis.

The selected eleven CalCOFI stations led to HS' and HSR estimates in good agreement with those obtained from remote sensing. The HS' mean rms difference and correlation for the region are $56 \times 10^7 J m^{-2}$ and 67% while for the HSR they are $98 W m^{-2}$ and 66%. Figure 12 shows the comparison at two of the selected stations. The satellite based estimates are corrected using *in situ* salinity measurements [Sato *et al.*, 1999].

The correlations in Figure 11 have a local minimum at 32.5°N, near the T/P crossover latitude. The presence of this minimum is independent of the haline correction considered (*in situ*, climatological or no correction). The presence of a continental margin does not seem to have as much influence in the correlation as it does on the rms difference. This indicates that the amplitude of the surface height may be incorrect but its phase is still reliable. Further corroboration of this hypothesis can be drawn from Figure 12: the correlation for the HSR is comparable to that estimated from the HS' itself.

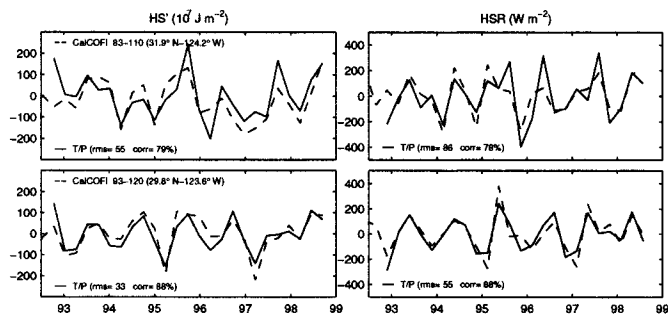


Figure 12. Comparison of the heat storage anomaly (left) and heat storage rate (right) between CalCOFI and T/P at selected stations, similar to Figure 7.

5. Concluding Remarks

Heat storage anomaly and heat storage rate are estimated at several locations from *in situ* measurements of temperature between 1992 to 1998. This period was chosen to coincide with the available T/P altimeter data. The total sea surface height measurements from satellite (corrected for the sea height anomaly due to haline effects) are correlated to the heat storage in the upper ocean by a linear relationship.

The *in situ* data came from four sites which provided relatively long ocean temperature time-series: the equatorial Pacific (TAO), tropical North Pacific (HOT), mid-latitude western Pacific (CalCOFI), and mid-latitude northwestern Atlantic (Hydrostation "S"). After data quality control and interpolation the temperature profiles were integrated to depths below the main thermocline. The long-term mean is removed from each time-series to obtain HS' which is compared to that estimated from the sea surface height anomaly from T/P.

The sea surface height anomaly signals from T/P are decomposed by the 2D FIR filter into three major components: a seasonal basin-scale non-propagating signal, a propagating signal, and a residual variability. The non-propagating signal reflects the fluctuations due to the seasonal heating and cooling of the upper ocean and long-term large-scale advective effects. The propagating signal is dominated by first-mode baroclinic Rossby waves and is subdivided into five period bands ranging from 45 days to two years. In addition to Rossby waves, the equatorial region shows eastward propagating Kelvin waves and westward propagating instability waves. The residual is divided into a meso-scale eddy field and a small-scale, high-frequency residual. The latter has a relatively small amplitude which is taken as an indication that most of the dynamical processes

associated with the variability of the T/P signal have been identified.

The Rossby wave aliasing problem (Sections 3.3.2 and 4.2.1) is to the best of our knowledge an original finding. This problem is more pronounced at high latitudes (higher than $\sim 35^\circ$) and affects estimates of amplitude, wavelength, and phase speed of first mode baroclinic Rossby waves. At certain latitudes it can even create eastward propagating aliased signals. This may explain some of the anomalous phase speeds previously observed in the T/P record [Chelton and Schlax, 1996].

The TAO region shows a high correlation between the heat storage estimated from *in situ* and T/P time-series. The rms differences are in average $54 \times 10^7 J m^{-2}$ and the mean correlation is 89%. This is an improvement over previous results [Chambers *et al.*, 1997], especially considering that the time-series used in this study have a temporal resolution of 10 days. The heat storage rates have a mean rms difference of $149 W m^{-2}$ and a mean correlation of 70%. The sea surface height anomaly in this region is dominated by the thermosteric non-propagating signal which near the Equator is responsible for approximately 75% of the T/P variability (Table 4). For instance, equatorial Rossby waves account for 13% at $0.5^\circ N$, while Kelvin waves account for 4% of the variability at the same latitude; instability waves account for up to 8% of the variability at $6.5^\circ N$. Towards higher latitudes the propagating signals become more important than the non-propagating ones. Accounting for the haline contribution to the sea surface height with climatology did not improve the results. For all other sites (Hydrostation "S", HOT and CalCOFI) local measurements of salinity were used [Sato *et al.*, 1999].

The comparison of HS' estimates from Hydrostation "S" near Bermuda and T/P shows an rms difference of $64 \times 10^7 J m^{-2}$ and a correlation coefficient of 83%. These results show a good agreement between the *in situ* and remotely sensed estimates, though they are inferior to those from the TAO region. In this location the rms difference between the HSRs is $207 W m^{-2}$ with a 73% correlation. Several factors favor the TAO estimates. Their temporal resolution is better (Table 1). There is less variability in terms of meso- to small-scale eddies in the Equatorial Pacific. Hydrostation "S" is relatively close to a small land mass (Bermuda Islands). Furthermore, the location of Hydrostation "S" coincides with a crossover latitude aggravating the Rossby wave aliasing problem. At this location the thermosteric signal accounts for 35% of the variance while Rossby waves are responsible for 29%. The Rossby wave spectrum is

dominated by a semiannual signal in the first two years, when the rms differences are larger due to the wave aliasing problem.

The analysis of the results from the HOT station points to many of the same problems addressed in the discussion of the Hydrostation "S" results. The rms difference is $54 \times 10^7 J m^{-2}$ and a correlation coefficient of 75% for the HS' and $223 W m^{-2}$ and 66% for the HSR. However, the main problem in this case is the temporal resolution of 40 days in a region where Rossby waves with a period of 90 days are responsible for 19% of the variance. The spectrum is dominated by planetary waves which account for 62% of the variance in contrast to 13% associated with non-propagating basin-scale signals (Table 6).

The mid-latitude northeastern Pacific (CalCOFI) data yields an average HS' rms difference of $56 \times 10^7 J m^{-2}$ and a correlation coefficient of 67%, while the HSR has an average rms difference of $98 W m^{-2}$ and a correlation of 66% in comparison with the T/P estimates. These results are obtained from 11 stations away from the continental slope. The correlation is the lowest of all studied sites. This is due in part to the proximity to the coast. In addition, the relatively long sampling period (90 days) and the presence of a crossover latitude within the sampled area detract from the results. On average at this location the planetary waves are predominant, explaining 35% of the variance, half of it in the semiannual band. The basin-scale thermal signal is responsible for 30% of the variance (Table 7).

The 2D FIR filtering procedure is a key piece of this method. It provides an accurate estimate of the heat storage and its rate of change from satellite data, and quantifies the relative participation of distinct physical processes in the heat storage fluctuations. Rossby waves are an important component of the heat storage variability at all studied sites, and they are the most energetic spectral component outside the equatorial region. Relatively less intense, significant Kelvin and instability waves are found in the TAO region. The contribution of the spectral band associated with meso-scale eddies increases poleward. This tendency is due to several factors: the presence of energetic western boundary currents; contamination because of increased wave aliasing; degradation of the filter's resolving power as planetary wavelengths become shorter and fast barotropic signals become more energetic [Thierney *et al.*, 1999; Stammer *et al.*, 1999].

This comparison with *in situ* data helps to validate the altimeter as a valuable tool to study climate-relevant variables in the ocean in detail. This study

underlines the importance of wide-spread long-term *in situ* measurements for the remote-sensing community as well as the necessity of a continuous monitoring of the sea surface height by satellite altimeters.

Appendix A: Two-Dimensional Finite Impulse Response Filters

The individual contributions of all but the last factor in Equation 6 are separated by the application of nonrecursive finite impulse response (FIR) filters [Jackson, 1986]. FIR filters are based on the convolution of two sequences, the original data, η , and the filter, f , resulting in the filtered data, η_f . In the present case $\eta(x, t)$ is a function of longitude and time, therefore the filter $f(i, j)$ is a function of the longitudinal lag i and temporal lag j . The filtered matrix $\eta_f(x, t)$ is obtained from:

$$\eta_f(x, t) = \sum_{i=-m}^m \sum_{j=-n}^n \eta(x+i, t+j) f(i, j). \quad (A1)$$

The filter for the components η_{t1} , η_{t2} and η_E is the Gaussian surface:

$$f(i, j) = \frac{e^{-\frac{1}{2}((\frac{\pi i}{m})^2 + (\frac{\pi j}{n})^2)}}{N}, \quad (A2)$$

$$\text{with } N \text{ such that } \sum_{i=-m}^m \sum_{j=-n}^n f(i, j) = 1.$$

The size of the filter, controlled by parameters m and n , is set to half-year and twice the basin width for η_{t1} . The filter is initially oversized to minimize the mixing of biannual and annual signals into the non-propagating component η_{t1} . After the Rossby wave signals are removed this filter is resized to half-year and 15° and applied a second time to yield η_{t2} . These parameters are set to avoid contamination by both Kelvin waves and aliased tidal signals. After the Kelvin wave signal is removed, the filter parameters are set to 50 days and 5° yielding η_E .

For the band-pass filtering of the Rossby wave components (η_{24} , η_{12} , η_6 , η_3) and the instability waves (η_1) the filter $f(i, j)$ is a Gaussian tapered cosinusoidal surface:

$$f(i, j) = \frac{e^{-\frac{1}{2}((\frac{\pi i}{m})^2 + (\frac{\pi j}{n})^2)}}{N} \cos\left(\frac{2\pi i}{L} - \frac{2\pi j}{T}\right) + M, \quad (A3)$$

$$\text{with } M \text{ and } N \text{ such that } \begin{cases} \sum_{i=-m}^m \sum_{j=-n}^n |f(i, j)| = 1, \\ \sum_{i=-m}^m \sum_{j=-n}^n f(i, j) = 0, \end{cases}$$

where L and T are the wavelength and period of the approximate center of each pass band. T is set to 730, 365, 183, 91, and 45 days and L is obtained from $L = c_p T$. The filter size parameters m and n are set to one period and one wavelength. The gaussian part of Equation A3 works as a smoother while the cosine part limits the power of the response to a specific area in the 2D spectrum. This can be understood as a 2D version of the tapered cosine window functions (Blackman, Hamming, Hanning, etc.) used in classical 1D spectral analysis, whose main advantages are the same: to minimize phase distortion and to reduce the amplitude of side-lobes (leaking).

For the band-pass filtering of η_K the filter $f(i, j)$ is composed of the positive elements of f in Equation A3, with M and N such that

$$\sum_{i=-m}^m \sum_{j=-n}^n f(i, j) = 1.$$

When filtering for η_K , T is set to 45 days and it is only applied between 5.5°S and 5.5°N, before filtering for η_E . This filter has a much broader pass band than those used for the Rossby wave components. This choice was taken because the eastward propagating signals are not as regular in period and wavelength as their westward counterparts.

An initial guess (indicated by the subscript 1) for the average zonal phase speed, c_{p1} as a function of latitude, is used to obtain L_1 from $L_1 = c_{p1} T_1$ with $T_1 = 730, 365, 183, 91$ and 45 days. The components of η_o are filtered in the following order: $\eta_{t1}, \eta_{24}, \eta_{12}, \eta_6, \eta_3, \eta_1, \eta_{t2}, \eta_K$ and η_E . Each band-passed signal is removed from the original data at every step before the next filter is applied, for example: η_{24} is obtained by filtering $\eta_o - \eta_{t1}$; η_{12} is obtained by filtering $\eta_o - \eta_{t1} - \eta_{24}$; η_6 is obtained by filtering $\eta_o - \eta_{t1} - \eta_{24} - \eta_{12}$; and so forth.

After the filter is applied to obtain each component, the filtered signal is multiplied by a constant factor g such that the variance of $(\eta - g\eta_f)$ is minimized. These filters are characterized by a smooth transition between the stop-bands and the pass-band, therefore some contamination among the wave signals can occur. To minimize this problem a fraction g_{ij} of the signal η_i is removed from η_j for all $j \neq i$. g_{ij} is such that the variance of $(\eta_j - g_{ij} \eta_i)$ is minimized.

The filters are applied to the $\eta_o(x, t)$ fields at every degree of latitude, using the initial values c_{p1}, T_1 and L_1 . The same c_{p1} is used for each of the Rossby wave bands. New values for the average c_p, L and T are estimated for each of the bands using a Radon transform

procedure based on Polito and Cornillon [1997]. One estimate is made for each area measuring T_1 by L_1 and the estimates are averaged in space and time to obtain a single value of c_p, L and T per latitude. The filtering procedure is then repeated using new parameters (but the same original data) until the average difference between c_p of the last loop and the present value of c_p has converged within 10% of the latter.

If during the iterations the filtered signal falls below 10% of the variance of its original signal, the filtered data is flagged and filtered once more with c_p as given by the initial guess. If the period of the filtered signal is within the range of the next band, the filtered data is flagged. If during the iterations the updated value of c_p differs from the initial guess by more than a factor of 2 while the amplitude remains above the 10% threshold, the loop is abandoned and the data is filtered once more with c_p as given by the initial guess and its results are flagged.

Acknowledgments. The authors would like to thank the reviewers of this manuscript.

References

- Benada, R., *Merged GDR TOPEX/Poseidon Users Handbook Version 2.0*, Jet Propulsion Lab. PO.DAAC, 1997, d-11007.
- Boulanger, J.-P., and C. Menkes, Propagation and reflection of long equatorial waves in the pacific ocean during the 1992-1993 El Niño, *J. Geophys. Res.*, **100**, 25,041–25,059, 1995.
- Chambers, D. P., B. D. Tapley, and R. H. Stewart, Long-period ocean heat storage rates and basin-scale heat fluxes from TOPEX, *J. Geophys. Res.*, **102**(C5), 10,525–10,533, 1997.
- Chambers, D. P., B. D. Tapley, and R. H. Stewart, Measuring heat storage changes in the equatorial Pacific: A comparison between TOPEX altimetry and tropical atmosphere-ocean buoys, *J. Geophys. Res.*, **103**(C9), 18,591–18,597, 1998.
- Chelton, D. B., and M. Schlax, Global observations of oceanic Rossby waves, *Science*, **272**, 234–238, 1996.
- Fu, L.-L., and R. A. Davidson, A note on the barotropic response of sea level to time-dependent wind forcing, *J. Geophys. Res.*, **100**, 24,955–24,963, 1995.
- Gill, A. E., and P. P. Niiler, The theory of the seasonal variability in the ocean, *Deep-Sea Res.*, **20**, 141–177, 1973.
- Halliwel, J., G. R., and P. Cornillon, Large-scale SST anomalies associated with subtropical fronts in the western North Atlantic during FASINEX, *J. Mar. Res.*, **47**, 757–775, 1989.
- Hsiung, J., R. E. Newell, and T. Houghtby, The annual cycle of oceanic heat storage and oceanic meridional heat transport, *Q. J. Roy. Meteor. Soc.*, **115**, 1–28, 1989.

- Jackson, L. B., *Digital Filters and Signal Processing*, Kluwer Academic Publishers, 1986.
- Karl, D. M., and R. Lukas, The Hawaii Ocean Time-series (HOT) Program: Background, rationale and field implementation, *Deep-Sea Res. II*, 43, 129–156, 1996.
- Kessler, W. S., Observations of long Rossby waves in the northern tropical pacific, *Technical Memorandum ERL PMEL-86*, NOAA, 1989, 169 pp.
- Levitus, S., and T. P. Boyer, World ocean atlas 1994, *Tech. Rep. Vol. 4*, National Oceanographic Data Center, Ocean Climate Laboratory, 1994, 117 pp.
- Lynn, R. J., and J. J. Simpson, The California current system: The seasonal variability of its physical characteristics, *J. Geophys. Res.*, 92(C12), 12,947–12,966, 1987.
- McPhaden, M. J., The Tropical Atmosphere Ocean array is completed, *Bull. Amer. Meteor. Soc.*, 76, 739–741, 1995.
- Moisan, J. R., and P. P. Niiler, The seasonal heat budget of the North Pacific: Net heat flux and Heat Storage rates (1950–1990), *J. Phys. Oceanogr.*, 28, 401–421, 1997.
- Polito, P. S., and P. Cornillon, Long baroclinic Rossby waves detected by TOPEX/POSEIDON, *J. Geophys. Res.*, 102, 3215–3235, 1997.
- Quiao, L., and R. H. Weisberg, Tropical instability wave kinematics: observations from the tropical instability wave experiment (TIWE), *J. Phys. Oceanogr.*, 100, 8677–8693, 1995.
- Sato, O. T., P. S. Polito and W. T. Liu, Importance of salinity measurements in the heat storage estimation from TOPEX/POSEIDON, submitted to *Geophysical Research Letters*, 1999.
- Schlax, M. G., and D. B. Chelton, Aliased tidal errors in TOPEX/POSEIDON sea surface height data, *J. Geophys. Res.*, 99, 24,761–24,775, 1994.
- Schrama, E. J. O., and R. D. Ray, A preliminary tidal analysis of TOPEX/POSEIDON altimetry, *J. Geophys. Res.*, 99, 24,799–24,808, 1994.
- Schroeder, E., and H. Stommel, How representative is the series of Panulirus stations of monthly mean conditions off Bermuda?, *Prog. Oceanogr.*, 5, 31–40, 1969.
- Stammer, D., C. Wunsch, and R. M. Ponte, De-aliasing of global high frequency barotropic motions in altimeter observations, submitted to *Geophysical Research Letters*, 1999.
- Thierney, C., J. Wahr, F. Bryan, and V. Zlotnicki, Short-period oceanic circulation: implications for satellite altimetry, submitted to *Geophysical Research Letters*, 1999.
- Wang, L., and C. Koblinsky, Can the TOPEX/POSEIDON altimetry data be used to estimate air-sea heat flux in the North Atlantic?, *Geophysical Research Letters*, 24(2), 139–142, 1997.
- Wang, L., and C. J. Koblinsky, Low frequency variability in the regions of the Kuroshio Extension and the Gulf Stream, *J. Geophys. Res.*, 100, 18,313–18,331, 1995.
- White, W. B., and C. K. Tai, Inferring interannual changes in global upper ocean heat storage from TOPEX altimetry, *J. Geophys. Res.*, 100, 24,943–24,954, 1995.
- Wyrski, K., and L. Urich, On the accuracy of heat storage computations, *J. Phys. Oceanogr.*, 12, 1411–1416, 1982.
- Yan, X. H., P. P. Niiler, S. K. Nadiga, R. H. Stewart, and D. R. Cayan, Seasonal heat storage in the North Pacific: 1976–1989, *J. Geophys. Res.*, 100(C4), 6899–6926, 1995.

P. S. Polito, O. S. Sato and W. Timothy Liu Jet Propulsion Laboratory, California Institute of Technology, MS 300-323, 4800 Oak Grove Dr., Pasadena CA 91109-8099. (e-mail: polito@pacific.jpl.nasa.gov; sato@pacific.jpl.nasa.gov; liu@pacific.jpl.nasa.gov)

Received August, 1999